

It has been argued that the Feni drift was deposited in a southerly derived counter-clockwise gyre in the Rockall trough, but this was based on the lack of evidence (before the drilling of well 214/4-1) for pre-Neogene (23 Myr ago) drift deposition north of the Wyville–Thomson ridge, and the assumption that the GSR was too shallow to allow deep-water exchange<sup>12</sup>. We suggest that the contemporaneous onset of drift deposition in both basins and the southwesterly flow direction obtained from the Southeast Faeroes drift implies that deep-water exchange must have started within the early Oligocene. The source of the deep water must have been northeast of the Southeast Faeroes drift, and a potential site could have been in a downwelling system in the Norwegian Sea<sup>5</sup>. This locus is consistent with the prevailing cooling in mid–high latitudes in the early Oligocene<sup>9</sup>, and as this northerly deep-water source would have been rich in biosiliceous components and initially poor in calcareous components<sup>9</sup> this would also explain the changes in biota observed in 214/4-1.

We therefore propose that the Southeast Faeroes drift is the earliest expression of NADW flow in the Faeroe–Shetland basin, during the early Oligocene. Its pathway into the open North Atlantic was directed southwest along the basin axis, crossing the Wyville–Thomson ridge into the northern Rockall trough. This is much earlier than the mid–late Miocene timing of deep-water marine connection that is used in current models of North Atlantic palaeocirculation<sup>2,7,11,12,27</sup>. The early onset of NADW formation could have contributed to an interhemispheric feedback mechanism similar to that suggested for the Quaternary<sup>28</sup> that would have helped stabilize Southern-Hemisphere cold climates at the end of the initial Antarctic glacial expansion in the earliest part of the Oligocene. □

Received 15 January; accepted 13 February 2001.

1. Broecker, W. S. The great ocean conveyor. *Oceanography* **4**, 79–89 (1991).
2. Schnitker, D. North Atlantic oceanography as possible cause of Antarctic glaciation and eutrophication. *Nature* **284**, 615–616 (1980).
3. Vogt, P. R. The Faeroe–Iceland–Greenland aseismic ridge and the western boundary undercurrent. *Nature* **239**, 79–81 (1972).
4. Eldholm, O. Paleogene North Atlantic magmatic-tectonic events: environmental implications. *Mem. Soc. Geol. Ital.* **44**, 13–28 (1990).
5. Miller, K. G. & Tucholke, B. E. in *Structure and Development of the Greenland–Scotland Ridge* (eds Bott, M. H. P., Saxov, S., Talwani, M. & Thiede, J.) 549–589 (Plenum, New York, 1983).
6. Thiede, J. & Eldholm, O. in *Structure and Development of the Greenland–Scotland Ridge* (eds Bott, M. H. P., Saxov, S., Talwani, M. & Thiede, J.) 445–455 (Plenum, New York, 1983).
7. Wold, C. N. Cenozoic sediment accumulation on drifts in the northern North Atlantic. *Paleoceanography* **9**, 917–941 (1994).
8. Wright, J. D. & Miller, K. G. Control of North Atlantic Deep Water circulation by the Greenland–Scotland Ridge. *Paleoceanography* **11**, 157–170 (1996).
9. Berggren, W. A. & Schnitker, D. in *Structure and Development of the Greenland–Scotland Ridge* (eds Bott, M. H. P., Saxov, S., Talwani, M. & Thiede, J.) 495–545 (Plenum, New York, 1983).
10. Berggren, W. A. & Hollister, C. D. in *Studies in Paleoceanography* (ed. Hay, W. W.) 126–186 (Society for Economic, Paleontology and Mineralogy, Tulsa, Oklahoma, 1974).
11. Schnitker, D. Global Paleocirculation and its deep water linkage to the Antarctic glaciation. *Earth Sci. Rev.* **16**, 1–20 (1980).
12. Stoker, M. S. in *Geological Processes on Continental Margins* (eds Stoker, M. S., Evans, D. & Cramp, A.) 229–254 (Geological Society, London, 1998).
13. Stow, D. A. V. & Holbrook, J. A. Hatton Drift contourites, northeast Atlantic. *Init. Rep. DSDP* **81**, 695–699 (1984).
14. Kidd, R. B. & Hill, P. R. Sedimentation on Feni and Gardar sediment drifts. *Init. Rep. ODP* **94**, 1217–1244 (1987).
15. Wold, C. N. in *The Tectonics, Sedimentation and Palaeoceanography of the North Atlantic Region* (eds Scrutton, R. A., Stoker, M. S., Shimmield, G. B. & Tudhope, A. W.) 271–302 (Geological Society, London, 1995).
16. Shor, A. N. & Poore, R. Z. Bottom currents and ice rafting in the North Atlantic. *Init. Rep. DSDP* **49**, 859–872 (1979).
17. Nilsen, T. H. in *Structure and Development of the Greenland–Scotland Ridge* (eds Bott, M. H. P., Saxov, S., Talwani, M. & Thiede, J.) 457–477 (Plenum, New York, 1983).
18. Heinrich, R., Wolf, T. C., Bohrmann, G. & Thiede, J. Cenozoic paleoclimatic and paleoceanographic changes in the northern hemisphere revealed by variability of coarse fraction composition in sediments from the Voring Plateau. *Proc. ODP Sci. Res* **104**, 75–188 (1989).
19. Mitchell, S. M. *et al.* in *Petroleum Geology of Northwest Europe: Proc. 4th Conf.* (ed. Parker, J. R.) 1011–1023 (Geological Society, London, 1993).
20. Davies, R., Cartwright, J. & Rana, J. Giant hummocks in deep-water marine sediments: Evidence for differential compaction and large-scale density inversion during early burial. *Geology* **27**, 907–910 (1999).
21. Boldreel, L. O. & Andersen, M. S. in *The Tectonics, Sedimentation and Palaeoceanography of the North Atlantic Region* (eds Scrutton, R. A., Stoker, M. S., Shimmield, G. B. & Tudhope, A. W.) 145–158 (Geological Society, London, 1995).

22. Hollister, C. D. & Heezen, B. C. in *Studies in Physical Oceanography* (ed. Gordon, A. L.) 37–66 (Gordon and Breach, New York, 1972).
23. Faugères, J.-C., Stow, D. A. V., Imbert, P. & Viana, A. Seismic features diagnostic of contourite drifts. *Mar. Geol.* **162**, 1–38 (1999).
24. Martini, E. Standard Tertiary and Quaternary calcareous nannoplankton zonation. *Proc. 2nd Plankton. Conf. Roma* **2**, 739–785 (1971).
25. Blow, W. H. *The Cainozoic Globigerinida* 1–1413 (Brill, Leiden, 1979).
26. Hein, J. R., Scholl, D. W., Barron, J. A., Jones, M. G. & Miller, J. Diagenesis of late Cenozoic diatomaceous deposits and formation of the bottom-simulating reflector in the southern Bering Sea. *Sedimentology* **25**, 144–181 (1978).
27. Dean, K., McLachlan, K. & Chambers, A. in *Petroleum Geology of Northwest Europe: Proc. 5th Conf.* (eds Fleet, A. J. & Boldy, S. A. R.) 533–544 (Geological Society, London, 1999).
28. Crowley, T. J. North Atlantic Deep Water cools the southern hemisphere. *Paleoceanography* **7**, 489–497 (1992).
29. Harland, W. B. *et al.* *A Geologic Time Scale 1989*. (Cambridge Univ. Press, Cambridge, 1990).

## Acknowledgements

We thank ExxonMobil International Ltd, Phillips Petroleum Company UK Limited, Marathon Oil UK Limited, Statoil (UK) Limited, Enterprise Oil plc, Anadarko North Sea Company, PanCanadian North Sea Limited, BPAmoco, Fugro-Geoteam, PGS Exploration (UK) Ltd and Westerngeco for permission to publish unreleased data. We thank T. Ramsay and C. Harris for discussion of the nannoplanktonic and microfossil record from well 214/4-1.

Correspondence and requests for materials should be addressed to R.D. (e-mail: richard\_davies@email.mobil.com) or J.C. (e-mail: cartwrightja@cardiff.ac.uk).

## Melt retention and segregation beneath mid-ocean ridges

Ulrich H. Faul

Research School of Earth Sciences, The Australian National University, Canberra, ACT 0200, Australia

Geochemical models of melting at mid-ocean ridges—particularly those based on trace elements and uranium-decay-series isotopes—predict that melt segregates from the matrix at very low porosities<sup>1–8</sup>, of order 0.1%. Some of these models also require that the melt ascends rapidly<sup>3,5</sup>. But these predictions appear to conflict with seismic data obtained by the mantle electromagnetic and tomography (MELT) experiment<sup>9</sup>. These data reveal, beneath the East Pacific Rise (at 17°S), a region of low velocities several hundred kilometres wide, which is best explained by the presence of 1–2% melt, distributed on a grain scale in disk-shaped geometries<sup>10</sup>. Here I show that these apparently contradictory constraints can be reconciled by taking into account the geometry and resulting permeability of the intergranular network of melt, together with the changing character of the melt as it ascends. A deep, volatile-rich melt with low viscosity and density is mobile at 0.1% porosity, but basaltic melt only becomes mobile at a porosity above 1%. While the volumetric contribution of the volatile-rich melt to the erupted basalts is small, the isotopic disequilibria (except for radium) generated by porous flow of this melt are preserved if melt transport is rapid at the onset of high-productivity melting. Also, because of incomplete extraction, some melt is retained in a broad zone, consistent with the MELT observations.

Because melt is generated on a grain scale, segregation of melt or fluid from the matrix begins with grain-scale porous flow. The permeability ( $k$ ) of porous rocks is generally calculated with

$$k = \frac{d^2 \phi^n}{C} \quad (1)$$

where  $d$  is the channel spacing (grain size),  $\phi$  is the melt/fluid

fraction with exponent  $n$  and  $C$  a constant. For porosities below 1%, the permeability is very sensitive to  $n$  (Fig. 1a).  $n = 2$  is calculated for a uniform network of cylinders<sup>11</sup> and an idealized isotropic model of the melt distribution in partially molten rocks<sup>12</sup>. However, for  $n = 2$ , the permeable network has to be self-similar at all porosities, whereas  $n = 3$  is obtained even for a network of cylinders with randomly varying diameters<sup>13</sup>. The relationship between permeability and porosity therefore depends on the behaviour of the network as a whole over a range of porosities; for the self-similar models to be applicable, the pore geometry needs to be close to ideal. Permeability measurements on hot-pressed aggregates of calcite and quartz with water as pore fluid<sup>14</sup>, yielding an exponent

of 3, show that even for texturally equilibrated rocks the pore geometry deviates significantly from the ideal case.

Comparison of the pore geometry in texturally equilibrated calcite with the melt geometry in dunite shows that the pore geometry in calcite is more regular. In calcite, triple-junction tubules account for most of the porosity, but triple-junction tubules contain only about 10% of the total melt content in partially molten dunite<sup>15</sup>. Network modelling<sup>13</sup> emphasizes that the size of the interconnecting throats (the narrowest passages in the pore space) controls the transport properties, even though the contribution of the throats to the overall porosity is less than that of nodal pores. In dunite, most melt resides in geometries best approximated by disks with an axial aspect ratio of 0.05 (ref. 10). The disks are connected by the network of triple-junction tubules, which control the permeability, until the disks become directly interconnected with increasing melt fraction, resulting in a sudden and substantial increase in permeability to values well above the tubule models.

Figure 1a shows a comparison of permeabilities calculated for a self-similar (idealized isotropic) channel network<sup>12</sup>, measured permeabilities<sup>14,16</sup> and experimentally determined melt inclusion shapes<sup>15</sup>. The permeabilities converge at higher porosities, but range over more than six orders of magnitude at 0.1% porosity. These permeabilities can be used to calculate melt-segregation velocities from equation (4) in ref. 17. Assuming the most favourable values for rapid segregation of basaltic melt (viscosity:  $\eta = 1$  Pa s; matrix density – melt density:  $\Delta\rho = 500$  kg m<sup>-3</sup>, values used throughout), segregation velocities for measured permeabilities<sup>14</sup> reach 10 cm yr<sup>-1</sup> at porosities between 1% and 1.5% and 1 m yr<sup>-1</sup> at 4%. Ascent velocities required by dynamic melting models<sup>3,5</sup> are above 1 m yr<sup>-1</sup> at porosities less than 0.5%; this can be achieved either with a melt

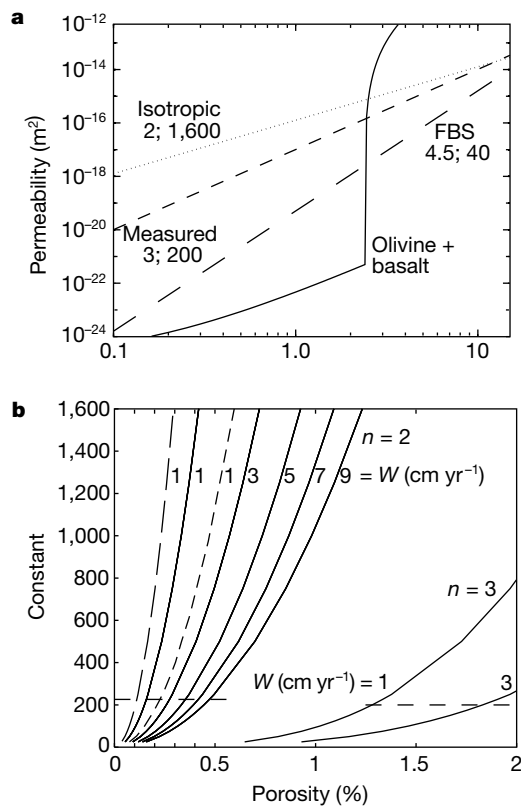


**Figure 1** Permeability and resulting maximum porosity in a one-dimensional melting column. **a**, Permeabilities at a grain size of 45  $\mu\text{m}$  calculated from a self-similar model (isotropic<sup>12</sup>), measured on texturally equilibrated rocks (measured<sup>14</sup>) and Fontainebleau sandstone (FBS<sup>16</sup>) and predicted for partially molten dunite (olivine+basalt<sup>15</sup>). The exponent and the constant for equation (1) are indicated; the larger the exponent the steeper the slope. For the system olivine plus melt that is below the interconnection threshold for disks, the permeability of the triple-junction tubule network is calculated with  $n = 3$  and  $C = 200$  up to a total melt fraction of 0.024 (melt fraction in triple-junction tubules is about 0.002; see Table 3 in ref. 15). Just below  $\phi = 0.025$  the disks interconnect and the permeability for  $\phi = 0.025$  and 0.033 is calculated from the data and equations given in ref. 15 for disk-shaped inclusions up to an aspect ratio of 0.15. At  $\phi = 0.033$ , nearly all melt inclusions belong to the percolation backbone; the permeability for the disks therefore levels off. The transition from very low permeability to steeply increasing permeability depends on the frequency of wetted two-grain boundaries. For a given porosity this frequency may be grain-size sensitive; it is possible that at mantle grain sizes the transition occurs at somewhat lower porosity than in the experiments. **b**, Maximum porosity at the top of a melting column versus the constant in equation (1) for  $n = 2$  and 3 and a range of solid upwelling velocities  $W$ . Extents of melting are 15% (solid lines) 7.5% (long dashes) and 30% (short dashes). The constants calculated for cylinders on a cubic grid<sup>11</sup> ( $C = 226$ ) and obtained from permeability measurements<sup>14</sup> ( $C = 200$ ) are indicated by horizontal dashed lines. The isotropic model<sup>12</sup> ( $C = 1,600$ , upper limit of **a**) yields porosities  $\geq 0.3\%$  even for slow upwelling and relatively small extents of melting; with measured permeabilities<sup>14</sup> the porosity always exceeds 1%.

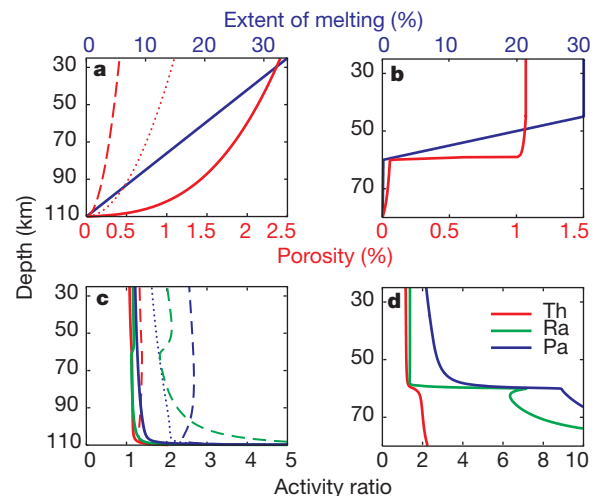


**Figure 2** Comparison of isotopic disequilibria produced by different permeabilities at a solid upwelling velocity of 3 cm yr<sup>-1</sup> and with distribution coefficients for an enriched source (Table 1). **a, c**, Standard permeability models have the same melting column as in ref. 4. Only if melt were distributed in cylinders on a cubic grid<sup>11</sup> (dashed lines) could significant excesses be produced by equilibrium porous flow models. With permeabilities measured on texturally equilibrated rocks<sup>14</sup> (solid lines) the porosity very quickly exceeds 1% (constraining the residual porosity in fractional melting models to  $>1\%$ ) and excesses decay within the first kilometre of flow. Th and Ra excesses calculated with the isotropic model (dotted line) are omitted for clarity; they lie below Pa. **b, d**, In the threshold model a small amount of volatile-rich melt is produced 20 km below the garnet–spinel transition, where high-productivity melting begins. Th and Pa excesses are preserved if the melt velocity increases sufficiently rapidly to metres per year. Ra excesses decay within 1 km after the onset of high-productivity melting, where the porosity increases from below 0.1% to above 1%. To preserve significant Ra excesses ( $^{226}\text{Ra}/^{230}\text{Th} \approx 2$ ) the melt needs to enter a fast transport regime ( $\sim 10$  m yr<sup>-1</sup>, requiring 100% melting at  $W = 8$  cm yr<sup>-1</sup> in the one-dimensional model) within 1–2 km of leaving the low porosity regime.

**Table 1 Isotopic excesses calculated with a range of permeability models**

Permeability	MC (km)	F (%)	W (cm yr <sup>-1</sup> )	$\phi_{\max}$ (%)	<sup>230</sup> Th/ <sup>238</sup> U	<sup>256</sup> Ra/ <sup>230</sup> Th	<sup>231</sup> Pa/ <sup>235</sup> U
Measured	85, E	34	3	2.45	1.07	1.16	1.22
Idealized isotropic	85, E	34	1/3/5	0.63/1.09/1.41	1.23/1.18/1.14	1.56/1.33/1.25	1.91/1.59/1.47
Cylinders	85, E	34	3	0.4	1.32	2.01	2.56
Cylinders	45, D	18	3	0.3	1.14	1.71	1.85
Threshold	15, E	30	1/3/5	1.1/1.1/1.1	1.10/1.16/1.18	1.37/1.37/1.37	1.54/2.18/2.50
Threshold	15, D	30	5	1.1	1.07	1.23	2.03
Observed range (mid/maximum)					1.1/1.4	2/4	2/3.6

MC, length of the high-productivity melting column; F, extent of melting; E, 'enriched' source. Bulk distribution coefficients ( $\times 10^{-4}$ ) in the garnet field: U, 45; Th, 20; Pa, 1; in the spinel field: U, 43; Th, 34; Pa, 0.5; Ra, 0.01 throughout. Mineral modes and garnet coefficients are from ref. 5; clinopyroxene coefficients are from ref. 33). D, 'depleted' source (bulk distribution coefficients as in ref. 4). Standard permeability models have the same melting column set-up as ref. 4 (garnet–spinel transition at 60 km depth, cessation of melting at 25 km depth). Threshold models also have the garnet–spinel transition at 60 km depth; volatile-rich melting begins 20 km below, high-productivity melting at the garnet–spinel transition. The steep increase in  $k$  for the threshold models caps the maximum porosity near the threshold porosity.

with the properties of a carbonate melt or with the melt geometry of partially molten lherzolite identical to that of cylinders on a cubic grid.

Uranium-decay-series (<sup>238</sup>U–<sup>230</sup>Th–<sup>226</sup>Ra and <sup>235</sup>U–<sup>231</sup>Pa) disequilibria (excesses of daughter or parent in the erupted melting product resulting from fractionation of parent from daughter due to different melt–solid partition coefficients) measured in MORBs are often used to model mantle melting processes. The model developed by refs 2 and 18 includes the fluid dynamics of melt segregation, but instead of calculating the porosity in the melting column from the relevant material properties ( $k$ ,  $\eta$  and  $\Delta\rho$ ), these properties are implicitly determined by a maximum porosity, which can be chosen to satisfy the U-series data. Here the porosity throughout the melting column is calculated by directly solving equation (16) in ref. 18, with  $k$ ,  $\eta$  and  $\Delta\rho$  as independent input parameters. These calculations show that porosity is not a free parameter in melting models but has well defined physical limits, which together with the mass balance requirement constrain the amount of melt present in the mantle, as well as its ascent velocity.

The maximum porosity at the top of a one-dimensional melting column increases with increasing upwelling velocity and extent of melting (Fig. 1b): calculated isotopic disequilibria will therefore decrease (Table 1). Keeping the maximum porosity constant while varying the matrix upwelling velocity  $W$  (Table 1 in ref. 6) implies that  $k$ ,  $\eta$  and  $\Delta\rho$  vary with matrix upwelling velocity. In order to achieve a maximum porosity near 0.1% (to model Ra excesses<sup>7</sup>), the permeability of partially molten rocks needs to exceed that of cylinders on a cubic grid<sup>11</sup>; this is the most permeable model of a porous rock which can be physically realized.

The calculations above show that melt can only segregate at low porosities if its viscosity is substantially lower than that of basaltic

melt. Mid-ocean ridge basalt (MORB) glasses contain between 0.2 and 0.6 wt.% water<sup>19</sup> (regionally averaged) and between 0.2 wt% (ref. 20) up to 0.7 wt% CO<sub>2</sub>, equivalent to about 100–400 p.p.m. H<sub>2</sub>O and a similar amount of CO<sub>2</sub> in the MORB source. This suggests that a hydrous fluid with dissolved silica and carbonate components is present at depth below the anhydrous peridotite solidus<sup>21,22</sup>. These C–O–H–silicate fluids or volatile-rich melts become interconnected at all porosities at pressures greater than about 2 GPa (ref. 23). Volatile-dominated melt will have low viscosity and low density, similar to carbonate melt<sup>24</sup>, which is also well interconnected in an olivine matrix<sup>25</sup>. Owing to the incompatibility of trace elements and U-series isotopes in the crystalline matrix, they will preferentially partition into any fluid or melt phase. The potential importance of a mobile, volatile-rich melt has been discussed before<sup>17,26–28</sup>; however, basaltic melt was also predicted to segregate rapidly at porosities below 1% (refs 17, 28).

The strong dependence of the calculated isotopic disequilibria on melt and matrix properties is illustrated in Fig. 2. In model calculations essentially identical to those of refs 4, 6 and 7 (Fig. 2a and c) significant excesses can only be produced if all melt is contained in uniformly varying cylinders on a cubic grid. With measured permeabilities the excesses decay soon after the first melt is formed, as the porosity rapidly exceeds 1%. With a volatile-rich melt at very low porosities and a rapid increase in permeability above a threshold, Th and Pa excesses can be preserved, but require rapid melt production at the onset of high-productivity melting (Fig. 2b and d). Fast melt production could be due to melting of inhomogeneities (for example, pyroxenites<sup>29</sup>) or melt focusing from two or three dimensions<sup>30</sup>. Figure 2d also shows that it is not possible to generate significant Ra excesses by dynamic melting<sup>3</sup>. Ra excesses are only produced at very low porosities, and although in this model the melt velocity increases rapidly to several metres per year as porosity increases from ~0.1% to ~1%, Ra excesses decay already at the onset of this transition regime (see also ref. 7). It is therefore not possible to generate substantial Ra excesses by conventional mantle melting models, using physically reasonable parameters.

Melt also moves by porous flow in dunite channels, so the same constraints on permeability apply. Owing to the steep increase of the permeability in the threshold model, which caps the porosity near the threshold, the porosity in channels will be only slightly higher than in the adjacent areas.

The above discussion suggests that Ra excesses are produced in the shallow mantle. One possibility is the involvement of mantle exposed at the ocean floor (abyssal peridotite). The high Cl contents observed in ref. 31 in some melt inclusions in plagioclase in MORB may be the result of re-infiltration of melt into relatively cool mantle exposed to hydrothermal circulation. As only very few samples with measured high Ra excesses also have reported Cl analyses, this origin of Ra excesses is a hypothesis at present. However, the two samples with high Ra excess in ref. 4 for which Cl analysis are available have high Cl contents; the four samples with some of the largest

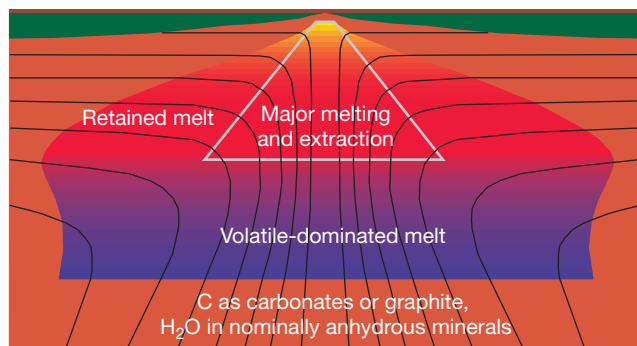


**Figure 3** Sketch of the distribution of melt beneath a mid-ocean ridge. The black lines indicate matrix flow lines for a corner flow model. Because melt extraction takes place above 1% porosity, some melt is retained when the matrix flow lines turn horizontal, resulting in the broad low velocity zone imaged by the MELT experiment. The region from which melt is extracted is much smaller (see for example ref. 27).

Ra excesses measured in MORB to date<sup>8</sup> all come from a graben in the Siqueiros Transform, which has undergone relatively recent extension.

The effect of variable viscosity and density on melt segregation beneath mid-ocean ridges is shown schematically in Fig. 3. A small amount of volatile-rich melt is formed in the upwelling part of the mantle by decarbonation reactions or by oxidation if carbon is stored as graphite or diamond. As water is incompatible in nominally anhydrous minerals relative to melt, it will partition into the melt, although the release might be gradual<sup>32</sup>. This volatile-rich melt is able to move at small porosities because of its low viscosity and density. Because the contribution of this melt to the volume of erupted basalts is small, its incompatible element-enriched character is lost, but isotopic disequilibria are not affected by dilution. Owing to incomplete extraction, some melt (more than 1%) remains in a broad zone, consistent with the observations from the MELT experiment. A two-stage melting model could also explain the depleted character of clinopyroxene in abyssal peridotites<sup>1</sup>. Modelling<sup>28</sup> showed that the observed rare earth element patterns require low porosities only at one stage but not throughout melt extraction. □

Received 15 September 2000; accepted 12 February 2001.

1. Johnson, K. H., Dick, H. J. B. & Shimizu, N. Melting in the oceanic upper mantle: An ion microprobe study of diopsides in abyssal peridotites. *J. Geophys. Res.* **95**, 2661–2678 (1990).
2. Spiegelman, M. & Elliott, T. Consequences of melt transport for uranium series disequilibrium in young lavas. *Earth Planet. Sci. Lett.* **118**, 1–20 (1993).
3. Richardson, C. & McKenzie, D. Radioactive disequilibria from 2D models of melt generation by plumes and ridges. *Earth Planet. Sci. Lett.* **128**, 425–437 (1994).
4. Lundstrom, C. C., Gill, J., Williams, Q. & Perfit, M. R. Mantle melting and basalt extraction by equilibrium porous flow. *Science* **270**, 1958–1961 (1995).
5. Salters, V. J. M. & Longhi, J. Trace element partitioning during the initial stages of melting beneath mid-ocean ridges. *Earth Planet. Sci. Lett.* **166**, 15–30 (1999).
6. Lundstrom, C. C., Williams, Q. & Gill, J. B. Investigating solid mantle upwelling rates beneath mid-ocean ridges using U-series disequilibria, 1: a global approach. *Earth Planet. Sci. Lett.* **157**, 151–165 (1998).
7. Lundstrom, C. C., Gill, J. & Williams, Q. A geochemically consistent hypothesis for MORB generation. *Chem. Geol.* **162**, 105–126 (2000).
8. Lundstrom, C. C., Sampson, D. E., Perfit, M. R., Gill, J. & Williams, Q. Insights into mid-ocean ridge basalt petrogenesis: U-series disequilibria from the Siqueiros Transform, Lamont Seamounts, and East Pacific Rise. *J. Geophys. Res.* **104**, 13035–13048 (1999).
9. The MELT Seismic Team. Imaging the deep seismic structure beneath a mid-ocean ridge: the MELT experiment. *Science* **280**, 1215–1218 (1998).
10. Faul, U. H., Toomey, D. R. & Waff, H. S. Intergranular basaltic melt is distributed in thin, elongated inclusions. *Geophys. Res. Lett.* **21**, 29–32 (1994).
11. Turcotte, D. L. & Schubert, G. *Geodynamics* (John Wiley, New York, 1982).
12. von Bargen, N. & Waff, H. S. Permeabilities, interfacial areas and curvatures of partially molten systems: Results of numerical computations of equilibrium microstructures. *J. Geophys. Res.* **91**, 9261–9276 (1986).
13. Zhu, W., David, C. & Wong, T.-f. Network modeling of permeability evolution during cementation and hot isostatic pressing. *J. Geophys. Res.* **100**, 15451–15464 (1995).
14. Wark, D. A. & Watson, E. B. Grain-scale permeabilities of texturally equilibrated, monomineralic rocks. *Earth Planet. Sci. Lett.* **164**, 591–605 (1998).
15. Faul, U. H. Permeability of partially molten upper mantle rocks from experiments and percolation theory. *J. Geophys. Res.* **102**, 10299–10311 (1997).
16. Bourbie, T. & Zinsner, B. Hydraulic and acoustic properties as a function of porosity in Fontainebleau sandstone. *J. Geophys. Res.* **90**, 11524–11532 (1985).
17. McKenzie, D. Some remarks on the movement of small melt fractions in the mantle. *Earth Planet. Sci. Lett.* **95**, 53–72 (1989).
18. Spiegelman, M. UserCalc: A Web-based uranium series calculator for magma migration problems. *Geochem. Geophys. Geosyst.* **1**, 1999 GC 0000 30 (2000).
19. Michael, P. Regionally distinctive sources of depleted MORB: Evidence from trace elements and H<sub>2</sub>O. *Earth Planet. Sci. Lett.* **131**, 301–320 (1995).
20. Zhang, Y. & Zindler, A. Distribution and evolution of carbon and nitrogen in the Earth. *Earth Planet. Sci. Lett.* **117**, 331–345 (1993).
21. Green, D. H. & Liebermann, R. C. Phase equilibria and elastic properties of a pyrolite model for the oceanic upper mantle. *Tectonophysics* **32**, 61–92 (1976).
22. Blundy, J. D., Brodholt, J. P. & Wood, B. J. Carbon-fluid equilibria and the oxidation state of the upper mantle. *Nature* **349**, 321–324 (1991).
23. Mibe, K., Fujii, T. & Yasuda, A. Connectivity of aqueous fluid in the Earth's upper mantle. *Geophys. Res. Lett.* **25**, 1233–1236 (1998).
24. Dobson, D. P. et al. In-situ measurement of viscosity and density of carbonate melts at high pressure. *Earth Planet. Sci. Lett.* **143**, 207–215 (1996).
25. Hunter, R. H. & McKenzie, D. The equilibrium geometry of carbonate melts in rocks of mantle composition. *Earth Planet. Sci. Lett.* **92**, 347–356 (1989).
26. Galer, S. J. G. & O'Nions, R. K. Magmagenesis and the mapping of chemical and isotopic variations in the mantle. *Chem. Geol.* **56**, 45–61 (1985).
27. Plank, T. & Langmuir, C. H. Effects of the melting regime on the composition of the oceanic crust. *J. Geophys. Res.* **97**, 19749–19770 (1992).

28. Kelemen, P. B., Hirth, G., Shimizu, N., Spiegelman, M. & Dick, H. J. B. A review of melt migration processes in the adiabatically upwelling mantle beneath oceanic spreading ridges. *Phil. Trans. R. Soc. Lond. A* **355**, 283–318 (1997).
29. Yaxley, G. M. Experimental study of the phase and melting relations of homogeneous basalt + peridotite mixtures and implications for the petrogenesis of flood basalts. *Contrib. Mineral. Petrol.* **139**, 326–338 (2000).
30. Asimow, P. D. & Stolper, E. M. Steady-state mantle–melt interactions in one dimension: I. Equilibrium transport and melt focusing. *J. Petrol.* **40**, 475–494 (1999).
31. Nielsen, R. L., Sours-Page, R. E. & Harpp, K. S. Role of a Cl-bearing flux in the origin of depleted ocean floor magmas. *Geochem. Geophys. Geosyst.* **1**, 1999 GC 0000 17 (2000).
32. Hirth, G. & Kohlstedt, D. L. Water in the oceanic upper mantle: implications for rheology, melt extraction and evolution of the lithosphere. *Earth Planet. Sci. Lett.* **144**, 93–108 (1996).
33. Wood, B. J., Blundy, J. D. & Robinson, J. A. C. The role of clinopyroxene in generating U-series disequilibrium during mantle melting. *Geochim. Cosmochim. Acta* **63**, 1613–1620 (1999).

**Acknowledgements**

Discussions with S. Eggins, D. Green and H. O'Neill are gratefully acknowledged, as well as pre-publication access to a G<sup>3</sup> article by M. Spiegelman. Reviews by T. Elliot and M. Spiegelman helped to shape this manuscript.

Correspondence and requests for materials should be addressed to the author (e-mail: uli.faul@anu.edu.au).

.....  
**Towards a general theory of biodiversity**

**Elizaveta Pachepsky\*†, John W. Crawford†, James L. Bown† & Geoff Squire\***

† SIMBIOS Centre, School of Computing, University of Abertay Dundee, Dundee DD1 1HG, UK

\* Vegetation Systems Unit, Scottish Crop Research Institute, Invergowrie, Dundee DD2 5DA, UK

.....  
 The study of patterns in living diversity is driven by the desire to find the universal rules that underlie the organization of ecosystems<sup>1,2</sup>. The relative abundance distribution, which characterizes the total number and abundance of species in a community, is arguably the most fundamental measure in ecology. Considerable effort has been expended in striving for a general theory that can explain the form of the distribution<sup>3,4</sup>. Despite this, a mechanistic understanding of the form in terms of physiological and environmental parameters remains elusive<sup>5</sup>. Recently, it has been proposed that space plays a central role in generating the patterns of diversity<sup>6,7</sup>. Here we show that an understanding of the observed form of the relative abundance distribution requires a consideration of how individuals pack in time. We present a framework for studying the dynamics of communities which generalizes the prevailing species-based approach to one based on individuals that are characterized by their physiological traits. The observed form of the abundance distribution and its dependence on richness and disturbance are reproduced, and can be understood in terms of the trade-off between time to reproduction and fecundity.

The relative abundance distribution describes how the individuals in a community are partitioned among rare and common species. A log-normal form of the distribution, implying a community containing many rare species and relatively few common ones, is associated with a community in equilibrium. A power-law (or geometric) form, implying a more equitable share of individuals amongst species groups, is associated with non-equilibrium behaviour resulting from perturbation due to disturbance, pollution or immigration<sup>8</sup>. Two pervasive theories—multiplicative recruitment<sup>3</sup> and sequential niche breakage<sup>4</sup>—attempt to explain the emergent log-normal form of the abundance distribution in general terms, but neither of these provides an explanation of the observed